



between the two cation sites, namely the content of cubic  $\text{CuFe}_2\text{O}_4$  and/or tetragonal  $\text{CuFe}_2\text{O}_4$ . Its structure diagram is as follows: Where the inverse is tetragonal  $\text{CuFe}_2\text{O}_4$ , and the normal is cubic  $\text{CuFe}_2\text{O}_4$ . Taking into consideration that the formation of spinel  $\text{CuCr}_2\text{O}_4$  greatly enhances the catalytic activity, we expect to observe a similar phenomenon in the Cu–Fe catalysts.

In this study, the Cu–Fe catalysts were prepared by an epoxide assisted route. The effect of calcination temperature was investigated for understanding the formation process of spinel  $\text{CuFe}_2\text{O}_4$  and transformation of the crystalline phase, which were proved by XRD and Mössbauer spectroscopy. The magnetic properties were also determined. As expected, all catalysts were ferromagnetic materials, which could benefit the separation and recycling processes. The catalytic activity of glycerol hydrogenolysis over Cu–Fe catalysts was tested. Cu–Fe was found to be a highly active and selective catalyst, upon which a glycerol conversion of 47% and a 1,2-propanediol selectivity of 92% were achieved at 190 °C, 4.1 MPa initial  $\text{H}_2$  pressure.

## Experimental

### Catalysts preparation

The Cu–Fe catalysts were synthesized by a sol–gel route.<sup>8,9</sup> In a typical synthesis, 2.9 g  $\text{Cu}(\text{NO}_3)_2 \cdot 3\text{H}_2\text{O}$  (AR, SINOPHARM, China) and 9.8 g  $\text{Fe}(\text{NO}_3)_3 \cdot 6\text{H}_2\text{O}$  (AR, SINOPHARM, China) with the desired molar ratio (Cu/Fe = 0.5) were dissolved in 47 mL ethanol (AR, SINOPHARM, China) at 60 °C. After adding 8 mL 1,2-propylene oxide (AR, SINOPHARM, China) to the solution, a brown transparent gel formed within a few minutes. The obtained wet gel was aged under air atmosphere and subsequently dried at 85 °C for 15 h. The resulting xerogel was calcined at the required temperature for 120 min. The prepared catalysts were designated as CuFe-*T*, where *T* denotes the calcination temperature.

### Characterization

The thermal behavior of samples was studied using thermogravimetric analysis (TG) and differential thermogravimetric analysis (DTG) conducted in a Mettler Toledo TGA/SDTA851e using an atmosphere of 20 vol%  $\text{O}_2$  in Ar with a temperature ramp rate of 10 °C  $\text{min}^{-1}$  from ambient temperature to 800 °C.

Nitrogen adsorption–desorption isotherms were measured by static  $\text{N}_2$  physisorption at 77 K with a Micromeritics 2020 surface area and porosimetry analyzer. Before the  $\text{N}_2$  physisorption measurement, all samples of approximately 0.1–0.2 g were heated to 150 °C under vacuum ( $10^{-3}$  Torr) for at least 3 h to remove adsorbed impurities. The specific surface area was calculated by the Brunauer–Emmett–Teller (BET) method. The total pore volume was derived from the adsorbed  $\text{N}_2$  volume at a relative pressure of approximate 0.99, and the Barrett–Joyner–Halenda (BJH) method was used to calculate the pore size distributions according to the desorption branch of the isotherms.

XRD patterns of the samples were measured in a D/MAX-2400 diffractometer with a Cu  $\text{K}\alpha$  monochromatized radiation source, operated at 40 kV and 100 mA. The average particle size was evaluated by the Scherrer formula from the half-width of the XRD diffraction peak corrected for instrumental broadening.

$$L = \frac{0.9\lambda_{\text{K}\alpha 1}}{B_{(2\theta)} \cos \theta_{\text{max}}}$$

where  $\lambda_{\text{K}\alpha 1}$  is 1.54178 Å, and  $B_{(2\theta)}$  is a full width at half-maximum of the diffraction peak in radians. The molar fraction *X* of each species in mixture was calculated from XRD patterns as<sup>16</sup>

$$X = \frac{S_i}{\sum_{i=1} S_i}$$

where  $S_i$  is the peak areas of the most intense reflections of each phase, respectively.

The magnetization was characterized by a superconducting quantum interference (SQUID, MPMSXL5) magnetometer with a maximum field of 15 kOe at 27 °C. Magnetic parameters such as saturation magnetization ( $M_s$ ), coercive force ( $H_c$ ) and residual magnetization ( $M_r$ ) were measured.

The <sup>57</sup>Fe Mössbauer spectra were recorded at room temperature using a Topologic 500 A spectrometer with a proportional counter. Moving <sup>57</sup>Co(Rh) in a constant acceleration mode was used as the radioactive source. All of the spectral analyses were conducted assuming a Lorentzian lineshape for computer folding and fitting. The Doppler velocity of the spectrometer was calibrated with respect to a-Fe foil. And the free recoil fraction was assumed to be the same for all iron species. In this way, Mössbauer parameters such as the isomer shift (IS), the electric quadrupole splitting (QS), the full linewidth at half maximum (LW), the magnetic hyperfine field (H), and the relative resonance areas of the different components of the absorption patterns (RI) were determined.

Temperature-programmed reduction (TPR) of the samples was carried out in a stream of 90 vol% argon and 10 vol% hydrogen with a flowing rate of 50 mL  $\text{min}^{-1}$ . The sample was heated from room temperature to 800 °C with a rate of 10 °C  $\text{min}^{-1}$ . The amount of the hydrogen consumption during the reduction was estimated with a thermal conductivity detector.

Copper metal surface area was calculated from a two-step analysis consisting of (i)  $\text{N}_2\text{O}$  oxidation of Cu to  $\text{Cu}_2\text{O}$  and (ii)  $\text{H}_2$  temperature-programmed-reduction of the formed  $\text{Cu}_2\text{O}$  surface species (s-TPR).<sup>17</sup> For the analysis, a Micromeritics autochem II 2910 automated catalyst characterization system equipped with a thermal conductivity detector (TCD) was used. Before the analysis, *in situ* pre-reduction of the copper phase to Cu(0) was performed at 300 °C in a flowing  $\text{H}_2$ –Ar mixture for 120 min (10 vol% at 30 mL  $\text{min}^{-1}$ ). The oxidation of Cu to  $\text{Cu}_2\text{O}$  by adsorptive decomposition of  $\text{N}_2\text{O}$  was carried out isothermally at 90 °C by a continuous flow of  $\text{N}_2\text{O}$ –He for 60 min (5 vol% at 20 mL  $\text{min}^{-1}$ ). After this process, s-TPR was carried out on the freshly oxidized  $\text{Cu}_2\text{O}$  surface in order to reduce  $\text{Cu}_2\text{O}$  to Cu. The reducing gas (10 vol%  $\text{H}_2$ –Ar at a flow rate of 30 mL  $\text{min}^{-1}$ ) entered into the reactor and a thermal conductivity detector (TCD) measured the amount of  $\text{H}_2$ -uptake. The heating rate of 10 °C  $\text{min}^{-1}$  from 40 to 800 °C was used. Quantitative  $\text{H}_2$ -uptakes were evaluated by integration of the collected s-TPR curves.

Cu metal surface area, MSA, and average copper particle size,  $\varnothing_{\text{av}}$  were calculated. Metal surface area was calculated as:  $\text{MSA} (\text{m}^2 \text{g}^{-1} \text{Cu}) = \text{Mol}_{\text{H}_2} \times \text{SF} \times \text{NA} / 10^4 \times \text{CM} \times W_{\text{Cu}}$ , where  $\text{Mol}_{\text{H}_2}$ , SF, NA, CM, and  $W_{\text{Cu}}$  are moles of hydrogen

experimentally consumed per unit mass of catalyst ( $\mu\text{mol H}_2 \text{ g}^{-1}_{\text{cat}}$ ), stoichiometric factor (2), Avogadro's number ( $6.022 \times 10^{23} \text{ mol}^{-1}$ ), number of surface Cu atoms per unit surface area ( $1.47 \times 10^{19} \text{ atoms m}^{-2}$ ), and Cu content (wt%), respectively. The O/Cu ratio is assumed to be 1/2 ( $\text{SF} = 2$ ) on the basis of UPS results.<sup>18</sup> Average copper particle size was calculated as:  $\varnothing_{\text{av}} \text{ (nm)} = 10^7 \times \text{SK} \times \text{CM} \times W_{\text{Cu}} / \text{SF} \times \text{Mol}_{\text{H}_2} \times \text{NA} \times \rho_{\text{Cu}}$ , where SK is a constant depending on Cu particle shape (6 or 5) and  $\rho_{\text{Cu}}$  is the density of copper ( $8.92 \text{ g cm}^{-3}$ ).

### Catalytic evaluation

Glycerol catalytic conversion was performed in a 50 mL stainless steel autoclave with a mechanical stirrer and an electric temperature controller, operated under  $\text{H}_2$  pressure of 4.1 MPa at 190 °C for 10 h. Prior to reaction, the as-prepared catalysts were reduced by 10 vol%  $\text{H}_2$  in Ar at 300 °C for 2 h in a fluidized bed reactor. About 20 mL aqueous solution of 60 wt% glycerol, and 5 wt% (based on glycerol) of the catalysts were charged into the autoclave. The reactor was sealed and pressurized to the required hydrogen pressure, and then heated to the test temperature. After the reaction, the autoclave was cooled to ambient temperature, then brought to atmospheric pressure, and then opened to allow the reaction mass to be discharged and centrifuged for removing the catalyst. The liquid products were analyzed with a Bruker 450-GC gas chromatograph equipped with a flame ionization detector (FFAP column: 30 m  $\times$  0.32 mm  $\times$  0.5  $\mu\text{m}$ ). While the gas products were analyzed with a 7890F gas chromatograph equipped with thermal conductivity detector (TDX-01 column: 4 mm  $\times$  2 m). The conversion of the glycerol is defined as follows:

$$\text{conversion(\%)} = \frac{\text{sum of moles of all products}}{\text{sum of moles of reactant}} \times 100\%$$

The selectivity to each product is defined as a selectivity based on carbon, where

$$\text{selectivity(\%)} = \frac{\text{moles of carbon in specific product}}{\text{moles of carbon in all products}} \times 100\%$$

### Results and discussion

As shown in Fig. 1, over the temperature range from ambient to 300 °C, there was a continuous weight loss (about 45%) in the TG curve. Further weight loss was not obvious when the temperature increased from 300 to 800 °C (*ca.* 3%), which was likely due to the formation of a crystallized  $\text{CuFe}_2\text{O}_4$  phase and the phase transformation from cubic  $\text{CuFe}_2\text{O}_4$  to tetragonal,<sup>19</sup> resulting in the released of lattice oxygen. The first discrete region of thermal decomposition can be observed in the DTG curve in the range of room temperature –115 °C, which is attributed to the elimination of crystallization water from precursors and release of 1,2-propylene oxide.<sup>9</sup> Heating up to 300 °C, the second thermal decomposition was due to the decomposition of Cu and Fe species and the formation of CuO and  $\text{Fe}_2\text{O}_3$ .

The XRD patterns of Cu–Fe catalysts calcined at different temperatures are depicted in Fig. 2. After thermal treatment at 400 °C, only one low broad diffraction peak was observed, corresponding to  $\alpha\text{-Fe}_2\text{O}_3$  (JCPDS 33-0664). This indicates the possible

formation of copper oxides in the amorphous state as evidenced by the TG results. As calcination temperature increased, good crystalline  $\text{CuFe}_2\text{O}_4$  phase (major phase) and trace amount of CuO (JCPDS 44-0706) and  $\alpha\text{-Fe}_2\text{O}_3$  were identified in the XRD pattern. The two peaks corresponding to (211) and (103) diffractions of tetragonal  $\text{CuFe}_2\text{O}_4$  (JCPDS 34-0425), at  $2\theta \approx 34.7^\circ$  and  $35.9^\circ$ ,<sup>6</sup> merge into a single broad peak, which is ascribed to the strong diffraction peak of the cubic  $\text{CuFe}_2\text{O}_4$  phase (JCPDS 25-0283) ( $2\theta \approx 35.6^\circ$ ). The molar fraction of ion species in a (t- $\text{CuFe}_2\text{O}_4$ )-(c- $\text{CuFe}_2\text{O}_4$ )-( $\alpha\text{-Fe}_2\text{O}_3$ ) mixture was calculated from XRD patterns as shown in Table 1. About 38% of c- $\text{CuFe}_2\text{O}_4$ , 50% of t- $\text{CuFe}_2\text{O}_4$  and 12% of  $\alpha\text{-Fe}_2\text{O}_3$  were obtained in CuFe-500 catalyst. Nevertheless, as for the CuFe-600 catalyst, the fraction of c- $\text{CuFe}_2\text{O}_4$  decreased to 31%, and accordingly that of t- $\text{CuFe}_2\text{O}_4$  increased to 60%, the rest was 9%  $\alpha\text{-Fe}_2\text{O}_3$ . This result indicated that a transformation process from the cubic  $\text{CuFe}_2\text{O}_4$  phase to the tetragonal phase occurred, which was in good agreement with the TG-DTG results. The transformation of  $\text{CuFe}_2\text{O}_4$  spinel from tetragonal to cubic phase was an exothermic behavior, which was confirmed by the TG-DSC results,<sup>20</sup> the opposite process was an endothermic behavior. Thus, high temperature favored the formation of the tetragonal phase. Nedkov *et al.* also considered the formation of the cubic structure of  $\text{CuFe}_2\text{O}_4$  at temperatures below 337 °C and the tetragonal above 437 °C.<sup>21</sup> Tsoncheva *et al.* demonstrated that the phase composition of the obtained product strongly depends on the annealing temperature, with a tendency to favor the tetragonal structure formation over the cubic one at higher temperatures.<sup>22</sup> A higher temperature for phase transformation is required in our study, which depends on the catalyst preparation method, however, it is reasonable. In addition, the higher the calcination temperature, the sharper the diffraction peaks, indicating a greater degree of crystallinity and crystallite growth, which was proved by the increased particle sizes in Table 1.

BET surface areas, pore volumes and mean pore sizes are listed in Table 2. As suggested in the XRD results, the surface area sharply decreased with increasing calcination temperature due to the increase of particle size and crystallinity. The pore volume exhibited the opposed tendency, while the mean pore size in the range of mesoporous was observed, provided by the framework of ion species in the sol-gel process. Under low calcination

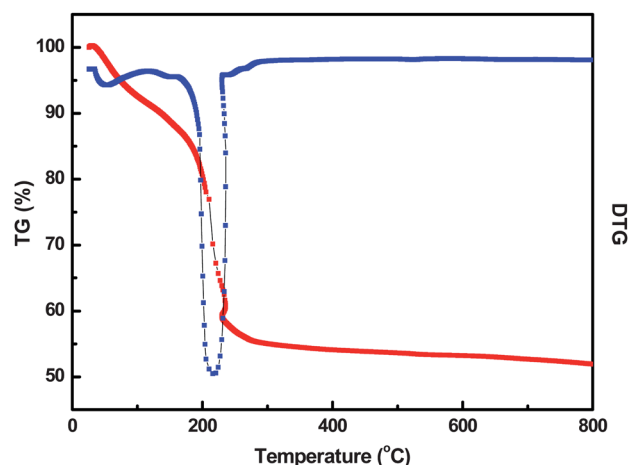
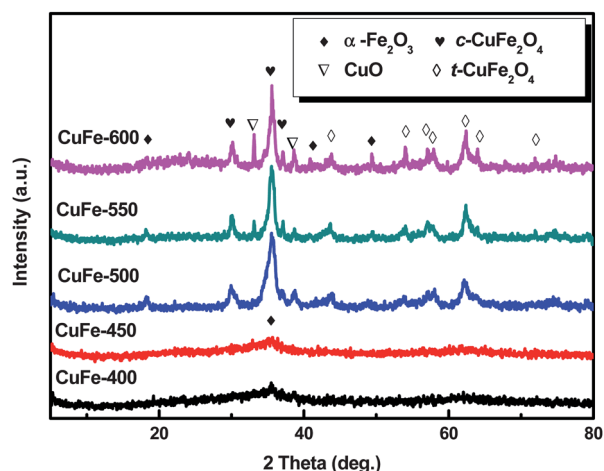


Fig. 1 TG/DTG curves of Cu–Fe dried gel sample.



**Fig. 2** The XRD patterns of Cu–Fe catalysts calcined at different temperatures.

temperatures, the formed CuO present in the framework, resulting in the small pore size. With increasing temperature, CuO was transferred into Fe<sub>2</sub>O<sub>3</sub>, which further formed spinel CuFe<sub>2</sub>O<sub>4</sub>, leading to an increase in pore size. The decrease of pore size was likely due to the increase of particle sizes or collapse of large pores.

The plots of magnetization ( $M$ ) as a function of applied field ( $H$ ) helps to understand the magnetic response of materials, and provides information about the magnetic parameters, such as saturation magnetization ( $M_s$ ), coercivity ( $H_c$ ) and remanence magnetization ( $M_r$ ). For easy discussion, the magnetic properties of the Cu–Fe catalysts are listed in Table 3. The obtained hysteresis loops (Fig. 3) show a normal S-shape type. The size and shape of hysteresis curves for a magnetic material are of considerable practical importance. The loop suggests a significant content of ferromagnetic materials. The ‘thickness’ of the middle of the S-shaped loop describes the amount of hysteresis, which is related to the coercivity of the material. The ratio of the remanent to the saturation magnetization ( $M_r/M_s$ ) was decreased at the beginning, and then increased as the calcination temperature increased, since that was related to the inter- and intra-grain exchange interactions, sub-lattice magnetization, magnetic anisotropy and morphology of the tested sample.<sup>23</sup> It can be further noticed that the  $M_r/M_s$  ratio for the CuFe-600 catalyst is very close to the ideal 0.5 value characteristic of single-domain noninteracting particles. The large reduction of this ratio in the CuFe-400 and CuFe-500 catalysts provide evidence to support their significant superparamagnetic behavior.<sup>24</sup>

**Table 1** The average particle sizes and molar fraction of ion species for CuFe- $T$  catalysts obtained from XRD patterns

Sample	$D$ (nm) $\pm 2$				Molar fraction <sup>a</sup> (%)		
	t-CuFe <sub>2</sub> O <sub>4</sub>	c-CuFe <sub>2</sub> O <sub>4</sub>	CuO	$\alpha$ -Fe <sub>2</sub> O <sub>3</sub>	t-CuFe <sub>2</sub> O <sub>4</sub>	c-CuFe <sub>2</sub> O <sub>4</sub>	$\alpha$ -Fe <sub>2</sub> O <sub>3</sub>
CuFe-400	—	—	—	2	—	—	—
CuFe-450	—	—	—	3	—	—	—
CuFe-500	7	8	10	7	50	38	12
CuFe-550	16	10	20	16	58	33	9
CuFe-600	20	10	24	22	60	31	9

<sup>a</sup> Molar fraction of ion species in the mixture of t-CuFe<sub>2</sub>O<sub>4</sub>, c-CuFe<sub>2</sub>O<sub>4</sub> and  $\alpha$ -Fe<sub>2</sub>O<sub>3</sub>.

**Table 2** BET surface area, pore volume and mean pore size for CuFe- $T$  catalysts

Samples	Surface area (m <sup>2</sup> g <sup>-1</sup> )	Pore volume (cm <sup>3</sup> g <sup>-1</sup> )	Mean pore size (nm)
CuFe-400	205	0.3	3.8
CuFe-500	54	0.2	9.5
CuFe-600	13	0.05	7.8

**Table 3** The magnetic properties of Cu–Fe catalysts calcined at different temperatures

Sample	$M_s$ (emu g <sup>-1</sup> )	$M_r$ (emu g <sup>-1</sup> )	$M_r/M_s$	$H_c$ (Oe)
CuFe-400	15.53	4.81	0.31	431
CuFe-500	17.13	0.99	0.06	70
CuFe-600	20.80	9.54	0.46	828

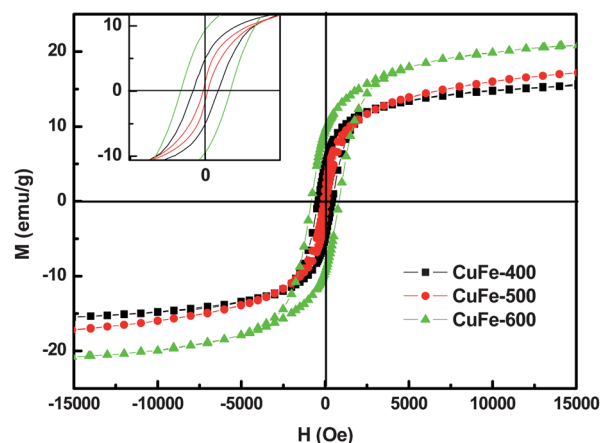


**Fig. 3** Magnetic hysteresis curves for the Cu–Fe catalysts calcined at different temperatures.

Although the saturation magnetization of  $\alpha$ -Fe<sub>2</sub>O<sub>3</sub> was high,<sup>25</sup>  $\alpha$ -Fe<sub>2</sub>O<sub>3</sub> in the CuFe-400 catalyst with a low degree of crystallinity and small particle size, resulted in lower saturation magnetization compared to the CuFe-500 catalyst. Obviously, this was also related to the change of phases. In the case of CuFe-500 and CuFe-600 catalysts, the main crystalline phases of the cubic and tetragonal CuFe<sub>2</sub>O<sub>4</sub> existed. This is because of a cooperative Jahn–Teller effect arising from the octahedral cupric ions.<sup>26</sup> The resulting structure may be represented by

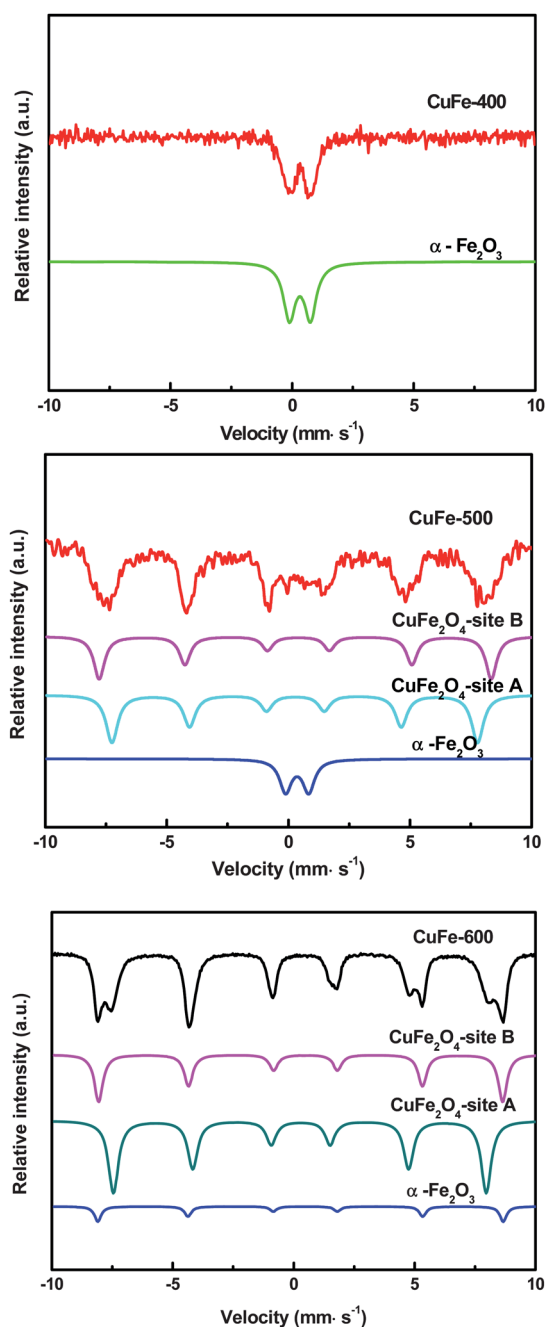


Fig. 4 Mössbauer spectra of Cu–Fe catalysts calcined at different temperatures.

Table 4  $^{57}\text{Fe}$  Mössbauer parameters of Cu–Fe catalysts calcined at different temperatures

Sample	State	IS ( $\text{mm}^{-1} \text{s}^{-1}$ )	QS ( $\text{mm}^{-1} \text{s}^{-1}$ )	H ( $\text{T}^{-1}$ )	RI (%)	LW ( $\text{mm}^{-1} \text{s}^{-1}$ )
CuFe-400	$\alpha\text{-Fe}_2\text{O}_3$	0.33	0.86	—	100	0.59
CuFe-500	$\text{CuFe}_2\text{O}_4\text{-Site B}$	0.35	-0.13	50.0	38.0	0.54
	$\text{CuFe}_2\text{O}_4\text{-Site A}$	0.27	-0.03	46.6	46.2	0.58
	$\alpha\text{-Fe}_2\text{O}_3$	0.35	0.95	—	15.8	0.58
CuFe-600	$\text{CuFe}_2\text{O}_4\text{-Site B}$	0.39	-0.20	51.8	33.3	0.43
	$\text{CuFe}_2\text{O}_4\text{-Site A}$	0.27	-0.03	47.8	58.3	0.49
	$\alpha\text{-Fe}_2\text{O}_3$	0.38	-0.19	52.0	8.4	0.34

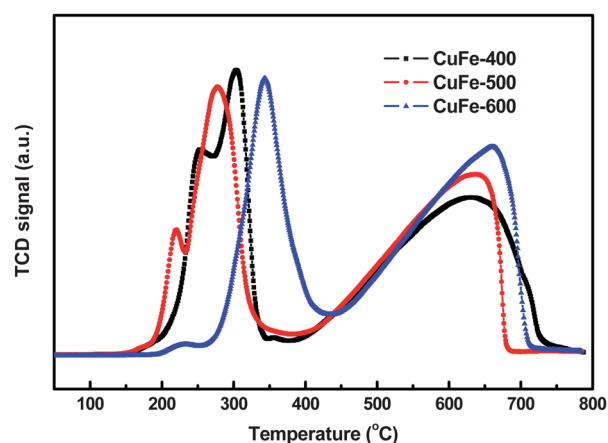


Fig. 5  $\text{H}_2$ -TPR profiles of Cu–Fe catalysts calcined at different temperatures.

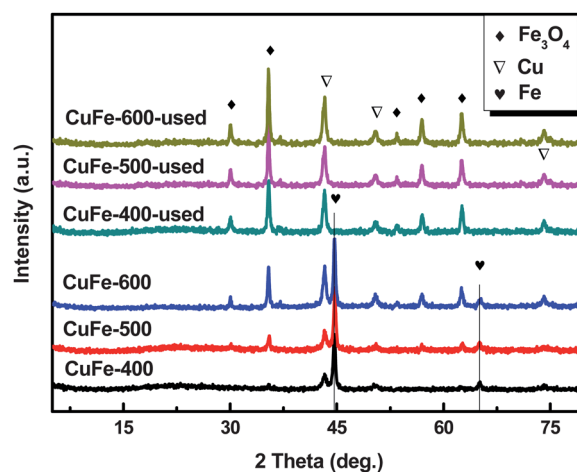
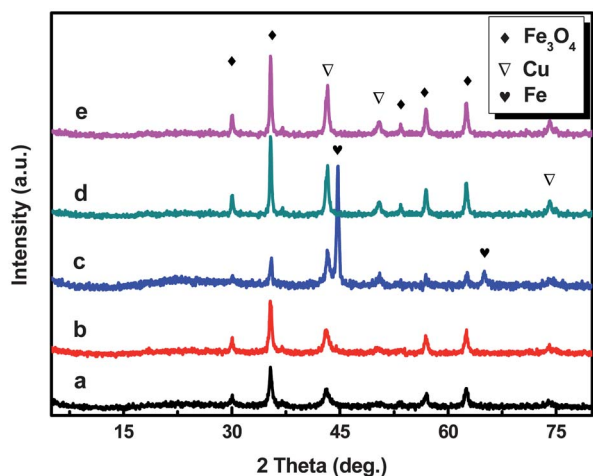


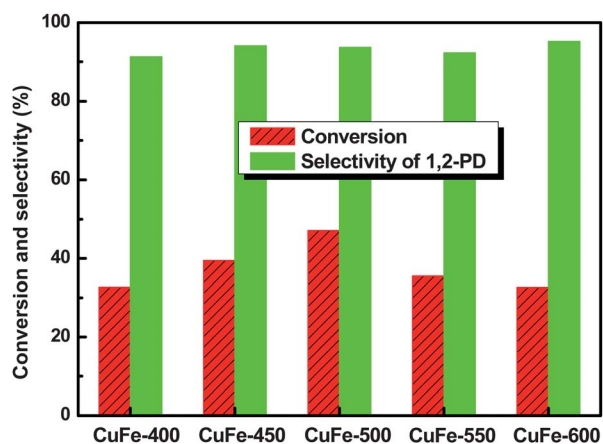
Fig. 6 The XRD patterns of CuFe-*T* catalysts after reduction at 300 °C and reaction.

Table 5 The average particle sizes and content of each phase for CuFe-*T* catalysts after reduction at 300 °C

Sample	<i>D</i> (nm) $\pm$ 2			Molar fraction (%)		
	$\text{Fe}_3\text{O}_4$	Fe	Cu	$\text{Fe}_3\text{O}_4$	Fe	Cu
CuFe-400	—	17	10	6	67	27
CuFe-500	18	19	16	11	59	30
CuFe-600	24	20	17	22	42	36



**Fig. 7** The XRD patterns of CuFe-500 catalysts reduced at 250 °C for 2 h (a), reduced at 300 °C for 0 h (b), reduced at 300 °C for 2 h (c), used (d) and used catalyst exposed to the air for 12 h (e).



**Fig. 8** Effect of calcination temperature on glycerol hydrogenolysis over Cu–Fe catalysts. (Reference conditions: 20 mL 60 wt% aqueous glycerol solution, 5 wt.% catalyst (based on glycerol), 190 °C, 4.1 MPa H<sub>2</sub>, 10 h, 900 r min<sup>-1</sup>).

$[\text{Cu}_x\text{Fe}_{1-x}]^A[\text{Cu}_{1-x}\text{Fe}_{1+x}]^B\text{O}_4$ , where  $x = 0$  and  $x = 1$  stand for the inverse and normal cases, respectively.<sup>24</sup> In  $\text{CuFe}_2\text{O}_4$ , the total saturation moment per formula unit,  $\mu_s$ , is related with the inversion degree  $\delta$  by  $\mu_s = \mu_{\text{Cu}} + 2\delta(\mu_{\text{Fe}} - \mu_{\text{Cu}})$ , where  $\mu_{\text{Fe}}$  and  $\mu_{\text{Cu}}$  are the  $\text{Fe}^{3+}$  and  $\text{Cu}^{2+}$  moments, respectively. Taking  $\mu_{\text{Fe}} = 5\mu_B$  and  $\mu_{\text{Cu}} = 1\mu_B$ , we have  $\mu_s = (8\delta + 1)\mu_B$ .<sup>24</sup> From XRD results, the tetragonal  $\text{CuFe}_2\text{O}_4$  phase was increased as calcination temperature rose to 600 °C, namely that the value of  $\delta$  was

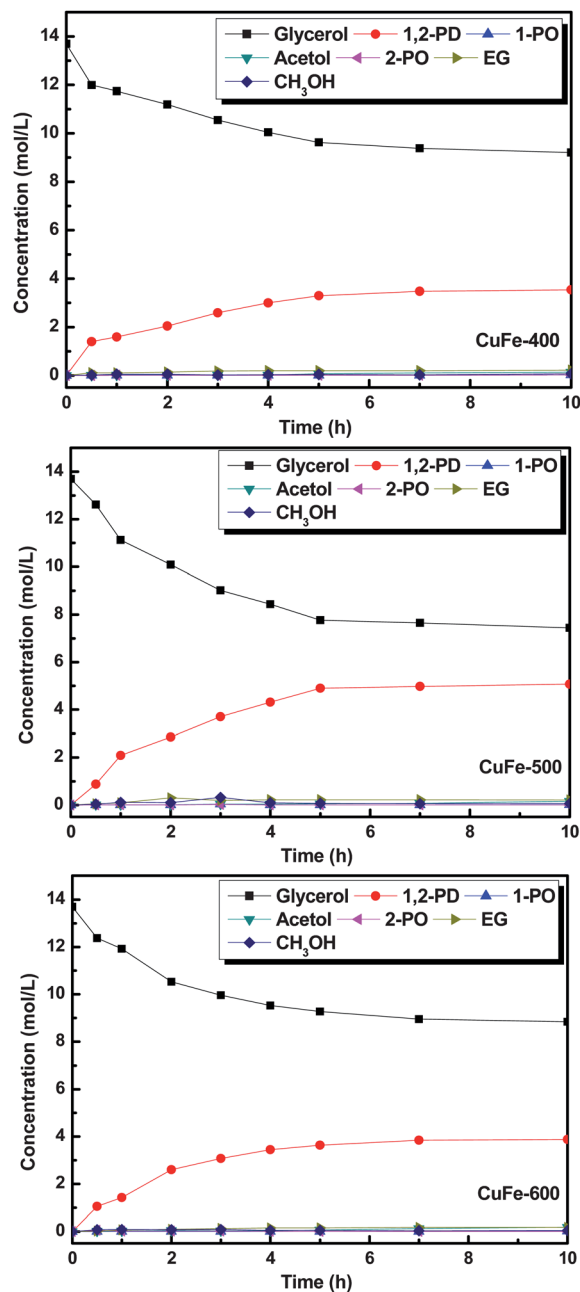


**Fig. 9** Concentration–time profiles for glycerol hydrogenolysis over Cu–Fe catalysts. (Reference conditions: 20 mL 60 wt% aqueous glycerol solution, 5 wt.% catalyst (based on glycerol), 190 °C, 4.1 MPa H<sub>2</sub>, 10 h, 900 r min<sup>-1</sup>).

**Table 6** Bulk and surface characteristics of the dispersed copper catalysts

Sample	Cu content <sup>a</sup> (wt%)	MSA (m <sup>2</sup> g <sup>-1</sup> Cu)	$\varnothing_{\text{av}}$ (nm)	Hydrogenolysis rate (mmol s <sup>-1</sup> mol <sup>-1</sup> Cu m <sup>2</sup> g <sup>-1</sup> )
CuFe-400	25.1	11.3	6.0	25.2
CuFe-500	24.7	4.9	13.8	83.8
CuFe-600	23.6	4.1	16.5	80.1

<sup>a</sup> Obtained by XRD results listed in Table 5.

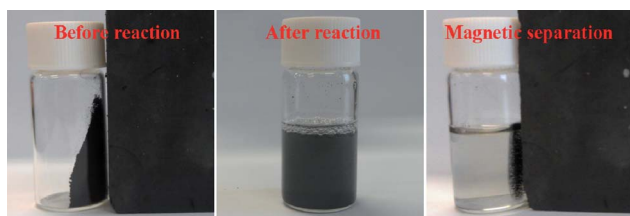


**Fig. 10** Images of magnetic characteristics and magnetic separation for CuFe-500 catalyst.

increased, resulting in an increase in the saturation moment. It is known that the moment is proportional to the saturation magnetization. Therefore, the higher saturation magnetization was observed for the CuFe-600 catalyst. Besides, the larger the particle size was, the higher the saturation magnetization was, which was attributed to surface effects as a result of finite-size scaling of the nano-crystallites.<sup>27</sup>

Mössbauer spectroscopy is a powerful tool to identify the oxidation states of iron, and the relative amount of different Fe species can be quantitatively determined. In our study, <sup>57</sup>Fe Mössbauer spectra were measured at room temperature. The results are shown in Fig. 4, with the hyperfine interaction parameters summarized in Table 4. The Mössbauer spectra of CuFe-400 could be fitted into an  $\alpha$ -Fe<sub>2</sub>O<sub>3</sub> doublet. It is known that, among the <sup>57</sup>Fe Mössbauer parameters, the IS value is the most important factor for diagnosing the chemical states of iron.<sup>28</sup> The Mössbauer spectra of IS = 0.33 mm s<sup>-1</sup> and QS = 0.86 mm s<sup>-1</sup> are in agreement with these value of  $\alpha$ -Fe<sub>2</sub>O<sub>3</sub>, as reported in ref. 29. As for the CuFe-500 sample, the Mössbauer spectrum is composed of two partially resolved magnetic sextets arising from Fe<sup>3+</sup> in tetrahedral (A) and octahedral (B) sites,<sup>24</sup> with a doublet of  $\alpha$ -Fe<sub>2</sub>O<sub>3</sub>. It was noteworthy that the Mössbauer spectrum of CuFe-600 sample could be fitted into three sextets. According to the Mössbauer spectrum of the CuFe-500 sample and XRD results, the sextets with RI = 33.3 and 58.3 could be attributed to CuFe<sub>2</sub>O<sub>4</sub>-Site B, and CuFe<sub>2</sub>O<sub>4</sub>-Site A, respectively. While the sextet with <sup>57</sup>Fe Mössbauer parameters of IS = 0.38 mm s<sup>-1</sup> and QS = -0.19 mm s<sup>-1</sup> accounted for about 8.4% and is attributed to  $\alpha$ -Fe<sub>2</sub>O<sub>3</sub>.<sup>30</sup> The change from doublet to sextet is due to the increase in particle size, which could be observed from XRD. Compared with the CuFe-500 catalyst, the RI ratio of CuFe<sub>2</sub>O<sub>4</sub>-Site A to Site B in CuFe-600 catalyst was increased, which was due to the migration of Fe<sup>3+</sup> ions from B sites to A sites and an increase in the degree of distortion, resulting in the increase of the t-CuFe<sub>2</sub>O<sub>4</sub> phase. This is in good agreement with the TG and XRD results. Since the Mössbauer parameters of t-CuFe<sub>2</sub>O<sub>4</sub> is very close to that of c-CuFe<sub>2</sub>O<sub>4</sub>, the fraction of

which is not determined. As is already known, the hyperfine field is proportional to magnetization. An increase of hyperfine field led to the increase of magnetization,<sup>20</sup> which was similar with the previous magnetic measurement. The CuFe-400 and CuFe-500 catalysts exhibited the superparamagnetic behavior in magnetic measurement, which was also proved by the presence of a doublet in Mössbauer spectrum, originating from  $\alpha$ -Fe<sub>2</sub>O<sub>3</sub> with small particle size.

The H<sub>2</sub>-TPR was also conducted to examine the reducibility of the Cu-Fe catalysts. The H<sub>2</sub>-TPR profiles of the Cu-Fe catalysts are depicted in Fig. 5. Each of the Cu-Fe samples exhibited two distinct peaks. For the CuFe-400 catalyst, the main peak (with a reduction temperature of ca. 304 °C) and the shoulder peak (with temperature of ca. 252 °C) were attributed to the reduction of  $\alpha$ -Fe<sub>2</sub>O<sub>3</sub> to Fe<sub>3</sub>O<sub>4</sub>, and CuO to metallic Cu, respectively.<sup>31</sup> For the others, the main peaks appeared in the temperature range of 250–400 °C, and were ascribed to the reduction of CuFe<sub>2</sub>O<sub>4</sub> to metallic Cu, and Fe<sub>2</sub>O<sub>3</sub>, and the subsequent reduction of Fe<sub>2</sub>O<sub>3</sub> to Fe<sub>3</sub>O<sub>4</sub>.<sup>31</sup> It is hard to define a clear boundary between each of the reduction steps. The weak shoulder peaks at about 220 °C were ascribed to the reduction of residual CuO with a good dispersion. While the peak appearing at a higher temperature (ca. 600 °C) for all catalysts could be assigned to the continuous reduction of the iron oxides to metallic Fe *via* FeO.<sup>32</sup> Obviously, compared with the CuFe-500 catalyst, the reduction peaks of the CuFe-600 catalyst was shifted to a higher temperature, which was ascribed to the transformation of cubic ferrite structure to the tetragonal one and/or the growth of crystallinity. This observation was in agreement with the XRD results.

In order to determine the structure of the catalysts after reduction, the XRD patterns of those samples are shown in Fig. 6. As expected, the characteristic diffraction peaks of Fe<sub>3</sub>O<sub>4</sub> and Cu were identified, moreover, their average particle size and molar fraction were also calculated, listed in Table 5. Surprisingly, the diffraction patterns of Fe with high intensity were observed, although the formation of Fe was favored at a high temperature of >400 °C (Fig. 5). This is likely to be due to a long reduction time at 300 °C. In order to prove this hypothesis, a short reduction time (maintained at 300 °C for 0 h) was conducted. No characteristic diffraction patterns of Fe were observed, as shown in Fig. 7. The lower reduction temperature (250 °C for 2 h) was also investigated, and no diffraction lines of Fe were identified.

Glycerol hydrogenolysis was used for evaluating the Cu-Fe catalysts under 4.1 MPa of hydrogen at 190 °C. Apart from the main product of 1,2-propanediol (1,2-PD), liquid products, such as 1-propanol (1-PO), 2-propanol (2-PO), acetol, ethylene glycol (EG), and methanol (CH<sub>3</sub>OH) were detected. Gas products, such

**Table 7** Recycling and stability of CuFe-500 catalyst<sup>a</sup>

Cycle number	Conversion (%)	Selectivity of 1,2-PD (%)	Leaching <sup>b</sup> (mg mL <sup>-1</sup> )	
			Cu	Fe
1	47	92	1.2 × 10 <sup>-3</sup>	0.46
2	42	93	8 × 10 <sup>-5</sup>	0.37
3	40	93	4 × 10 <sup>-5</sup>	0.28

<sup>a</sup> Reference conditions: 20 mL 60 wt.% aqueous glycerol solution, 5 wt.% catalyst (based on glycerol), 190 °C, 4.1 MPa H<sub>2</sub>, 10 h, 900 r min<sup>-1</sup>.

<sup>b</sup> Determined by inductively coupled plasma-optical emission spectroscopy (ICP-OES).

as CH<sub>4</sub>, CO and CO<sub>2</sub> with low selectivity and yield (<0.1%), were also identified. Therefore, we will only discuss the liquid products. The results of glycerol conversion and selectivity to 1,2-PD are shown in Fig. 8. The glycerol conversion as a function of catalyst calcination temperature shows a volcano shape. The conversion of glycerol was 33% on the catalyst calcined at 400 °C. It passed a maximum of 47% at 500 °C and dropped to 32% at 600 °C. Product distribution was not sensitive to the calcination temperature. 1,2-PD selectivity was maintained at about 92%. The CuFe-400 catalyst exhibited the lowest activity, even though it had the high copper metal surface area (Table 6). This result indicated that the formation of spinel CuFe<sub>2</sub>O<sub>4</sub> was able to greatly enhance the activity, as demonstrated in previous work.<sup>8,9</sup> The possible reason is that the metallic copper with high dispersion was formed through the epitaxy of Cu<sup>2+</sup> from spinel CuFe<sub>2</sub>O<sub>4</sub> during the reduction, resulting in the strong interaction between Cu and Fe<sub>3</sub>O<sub>4</sub>. The CuFe-600 catalyst gave the lower glycerol conversion compared to CuFe-500 catalyst, which was due to the lower copper metal surface area.

The concentration–time profiles for glycerol hydrogenolysis over the Cu–Fe catalysts are also shown in Fig. 9. According to these profiles, the hydrogenolysis rate was calculated. The CuFe-500 catalyst gave the highest hydrogenolysis rate. Compared with Cu–Cr catalysts in our previous work,<sup>8</sup> the same reactivity could be obtained over Cu–Fe catalyst under a lower reaction temperature. At the same temperature (210 °C), the conversion of glycerol was sharply increased from 47 to 81%, while the selectivity of 1,2-PD was significantly decreased (65%). Due to the excellent magnetism for Cu–Fe catalysts, the presented catalyst could be easily recycled as shown in Fig. 10.

The recycling procedure of the CuFe-500 catalyst was performed for examining the stability of the catalysts. After recycling the catalyst three times the glycerol conversion was decreased from 47% to 40%, while the selectivity of 1,2-PD was slightly increased. The decrease in conversion was due to the leaching of active copper as listed in Table 7. It was noteworthy that after recycling twice, the conversion was slightly decreased even though the leaching of iron was significant, indicating that the metal iron was not an active catalytic phase. For further proof, the hydrogenolysis of glycerol over the CuFe-500 catalyst with no phase of Fe<sup>0</sup> after reduction at 250 °C, was also conducted. About 46% conversion with 93% selectivity of 1,2-PD was obtained.

## Conclusion

Cu–Fe catalysts with stoichiometric proportions (Cu/Fe molar ratio is 0.5) have been synthesized by an epoxide assisted route. With increasing calcination temperature, the significant change of crystalline phases was observed from XRD results. Cubic and tetragonal CuFe<sub>2</sub>O<sub>4</sub> were presented in both CuFe-500 and CuFe-600 catalysts. And a transformation of crystalline phases from cubic to tetragonal CuFe<sub>2</sub>O<sub>4</sub> with elevating calcination temperature was determined by TG-DTG, XRD, and Mössbauer spectroscopy. The magnetic characterization showed that all catalysts had a ferromagnetic nature and the saturation magnetization values monotonously increased with increasing calcination temperature. In addition, the CuFe-400 and CuFe-500 catalysts exhibited significant superparamagnetic behavior,

which was proved by Mössbauer spectroscopy as the presentation of doublet. The catalytic performance of Cu–Fe catalysts was examined for the hydrogenolysis reaction of glycerol. It was found that the formation of spinel CuFe<sub>2</sub>O<sub>4</sub> could greatly enhance the activity. The Cu–Fe catalyst was found to be a highly active and selective catalyst, on which a glycerol conversion of 47% and a 1,2-propanediol selectivity of 92% were achieved at 190 °C, 4.1 MPa initial H<sub>2</sub> pressure for 10 h.

## Acknowledgements

We gratefully acknowledge the financial support provided by the National Natural Science Foundation of China (21073023 and 20906008) and the Fundamental Research Funds for the Central Universities (DUT12YQ03).

## Notes and references

- 1 S. W. Baek, J. H. Kim and J. Bae, *Solid State Ionics*, 2008, **179**, 1570.
- 2 R. W. Grimes, A. B. Anderson and A. H. Heuer, *J. Am. Chem. Soc.*, 1989, **111**, 1.
- 3 W. H. Bragg, *Philos. Mag.*, 1915, **30**, 305.
- 4 S. Nishikawa, *Proc. Tokyo Math.-Phys. Soc.*, 1915, **8**, 199.
- 5 Y. M. Z. Ahmed, M. M. Hessian, M. M. Rashad and I. A. Ibrahim, *J. Magn. Mater.*, 2009, **321**, 181.
- 6 J. Z. Jiang, G. F. Goya and H. R. Rechenberg, *J. Phys.: Condens. Matter*, 1999, **11**, 4063.
- 7 C. Liang, Z. Ma, L. Ding and J. Qiu, *Catal. Lett.*, 2009, **130**, 169.
- 8 Z. Ma, Z. Xiao, J. A. van Bokhoven and C. Liang, *J. Mater. Chem.*, 2010, **20**, 755.
- 9 Z. Xiao, Z. Ma, X. Wang, C. T. Williams and C. Liang, *Ind. Eng. Chem. Res.*, 2011, **50**, 2031.
- 10 S. Wang, Y. Zhang and H. Liu, *Chem.–Asian J.*, 2010, **5**, 1100.
- 11 M. Akiyama, S. Sato, R. Takahashi, K. Inui and M. Yokota, *Appl. Catal., A*, 2009, **371**, 60.
- 12 Z. Huang, F. Cui, H. Kang, J. Chen, X. Zhang and C. Xia, *Chem. Mater.*, 2008, **20**, 5090.
- 13 Z. Yuan, J. Wang, L. Wang, W. Xie, P. Chen, Z. Hou and X. Zheng, *Bioresour. Technol.*, 2010, **101**, 708.
- 14 F. Kenfack and H. Langbein, *Cryst. Res. Technol.*, 2004, **39**, 1070.
- 15 M. Yokoyama, A. Nakamura, T. Sato and K. Haneda, *J. Magn. Soc. Jpn.*, 1998, **22**, 243.
- 16 C. Liang, F. Tian, Z. Li, Z. Feng, Z. Wei and C. Li, *Chem. Mater.*, 2003, **15**, 4846.
- 17 A. Gervasini and S. Bennici, *Appl. Catal., A*, 2005, **281**, 199.
- 18 J. W. Evans, M. S. Wainwright, A. J. Bridgewater and D. J. Young, *Appl. Catal.*, 1983, **7**, 75.
- 19 S. Roy and J. Ghose, *J. Solid State Chem.*, 1999, **144**, 159.
- 20 S. Tao, F. Gao, X. Liu and O. T. Sørensen, *Mater. Sci. Eng., B*, 2000, **77**, 172.
- 21 I. Nedkov, R. E. Vandenberghe, T. Marinova, P. Thailhades, T. Merodiiska and I. Avramova, *Appl. Surf. Sci.*, 2006, **253**, 2589.
- 22 T. Tsoncheva, E. Manova, N. Velinov, D. Paneva, M. Popova, B. Kunev, K. Tenchev and I. Mitov, *Catal. Commun.*, 2010, **12**, 105.
- 23 K. V. P. M. Shafi, A. Gedanken, R. Prozorov and J. Balogh, *Chem. Mater.*, 1998, **10**, 3445.
- 24 G. F. Goya and H. R. Rechenberg, *Nanostruct. Mater.*, 1998, **10**, 1001.
- 25 H. Danan, A. Herr and A. J. P. Merer, *J. Appl. Phys.*, 1968, **39**, 669.
- 26 Ph. Tailhades, C. Villette and A. Rousset, *J. Solid State Chem.*, 1998, **141**, 56.
- 27 N. M. Deraz, *J. Alloys Compd.*, 2010, **501**, 317.
- 28 E. Murad and J. Cashion, *Mössbauer Spectroscopy of Environmental Materials and Their Industrial Utilization*, Kluwer Academic Publishers, Boston, MA, 1984, p. 19.
- 29 K. Liu, A. Q. Wang, W. S. Zheng, J. H. Wang, Y. Q. Huang, J. Y. Shen and T. Zhang, *J. Phys. Chem. C*, 2010, **114**, 8533.
- 30 E. Manova, T. Tsoncheva, D. Paneva, M. Popova, N. Velinov, B. Kunev, K. Tenchev and I. Mitov, *J. Solid State Chem.*, 2011, **184**, 1153.
- 31 L. Dong, Z. Liu, Y. Hu, B. Xu and Y. Chen, *J. Chem. Soc., Faraday Trans.*, 1998, **94**, 3033.
- 32 K. Faungnawakij, R. Kikuchi, T. Fukunaga and K. Eguchi, *Catal. Today*, 2008, **138**, 157.